Subsurface Reflectivity Reconstruction Schemas for a Holographic Airborne GPR Using Surface Geometry Data

Pedro Ramaciotti*†, Mario Durán‡ and Ricardo Hein‡
*Centre de Mathématiques Appliquées
Centre National de Recherche UMR 7641, Ecole Polytechnique
91128 Palaiseau Cedex, France.
†Departamento de Ingeniería de Minería
Escuela de ingeniería, Pontificia Universidad Católica de Chile
Av. Vicuña Mackenna 4860, Macul, Santiago, Chile.
‡Ingenieros Matemáticos Consultores Asociados S.A. (INGMAT)
José Miguel de la Barra 412, 4to Piso, Santiago, 8320110 Chile.

***Abstract*—The surface of a region under radar analysis, being possibly irregular, poses a challenge to many Ground Penetrating Radar (GPR) imaging techniques. This article describes different advances in the reconstruction of the subsurface electromagnetic reflectivity using an airborne GPR collecting a synthetic hologram. The approaches presented use explicit knowledge of the surface's geometry, acquired using complementary laser technologies, in order to include it in inversion schemas using a reconstructed and interpolated hologram structure obtained from the synthetic radar data. These schemas allow for the reconstruction of the subsurface electromagnetic reflectivity in regions with irregular surfaces using radar data acquired from airborne radars. Results for different scenarios and reconstruction schemas are presented using simulated data and real data acquired with a prototype of an airborne radar.**

I. Introduction

Ground Penetrating Radar (GPR) is a technology that finds multiple applications in different fields, such and geology, archeology, humanitarian demining, mining exploration, process inspection, among others. Particular applications include the detection and identification of underground structures, bodies of water, cavities, cracks, inclusions, undesired objects or defaults, landmines and unexploded ordnance under a given surface. Airborne GPR technologies can extend these applications into interesting or even necessary new frameworks: the safe detection of landmines, exploration in remote locations, the rapid analysis under large patches of surfaces, subsurface analysis in industrial processes that require non-intrusive (often contactless) inspection, among others.

GPR technologies can be divided in three main categories [8]: time-domain impulse radars, frequency-modulated continuous-wave radars and holographic radars. Holographic radars, on which the reported results are based, use a single frequency continuous wave in multi-monostatic configuration. They can achieve greater resolutions on a subsurface image plane, but on the other hand, they do not benefit from the possibility of time-varying gain to selectively amplify deeper reflections as impulse radars can [3][5]. These characteristics make the holographic GPR still a good candidate for numerous applications, such as landmine detection (e.g. [4]) and subsurface inspection in some industrial processes (e.g. [9]).

Holographic GPRs have been shown to provide excellent resolution capabilities when the antennanas can be placed on the surface, effectively possing the problem in one propagation domain. The situation changes in the case of airborne radars, where two propagation domains separated by an interface surface is the unavoidable setting. Some approaches have been successfully proposed, but considering a flat interface surface (e.g. [6],[7]), which leaves a wide range of interesting applications out. These proposed approaches include different imaging schemes with different computational complexities, and thus different degrees of applicability as real-time technologies.

In this article, we present an imaging scheme for the subsurface reflectivity using airborne GPRs across non-flat interface surfaces and an experimental prototype, featuring a LIDAR telemetry scanner allowing for the inclusion of the surface's geometrical shape into the imaging procedure. Firstly, a general setting of the subsurface imaging problem is established. Secondly, the principle of the imaging scheme is exposed. Then, the experimental setting is described. Finally, simulated and experimental results are presented as validation cases for the technology.

II. General Setting

The general setting of the subsurface imaging problems considered in this article consists of two propagation domains Ω_1 and Ω_2, above and below an interface surface Γ_S. A target Ω_3 to be detected is buried in Ω_2. The wavenumber k_1 and k_2 for the propagation domains are assumed to be known (specified in simulations or measured in physical experiments). In most settings, the propagation domain Ω_1 will be assumed to be open air in normal conditions with electrical permittivity

978-1-4799-6495-6/15/$31.00 ©2015 IEEE

$\varepsilon_1 = \varepsilon_0$, that of the vacuum, whereas the propagation domain Ω_2 will be assumed to be homogeneous with electrical permittivity $\varepsilon_2 = \varepsilon_r\varepsilon_0$, being ε_r the relative electrical permittivity. The physical properties of Ω_3 are assumed to contrast those of Ω_2 so as to produce significant backscattering perceivable by the radar system. Several antennas (or possibly the same in a synthetic assembly) radiate a monochromatic continuous wave of fixed frequency f (with an associated wavelength λ in Ω_1), in a multi-monostatic configuration, and measure the backscattered In-phase and Quadrature components. An emission/reception point $\vec{r}_H$ belongs to a surface Γ_H where the hologram is recorded, typically described by the movement of an antenna array. Fig. 1 shows the described setting for a general subsurface imaging problem.

Recorded In-phase and Quadrature measurements of the backscattered signal on points $\vec{r}_H$ are interpolated over Γ_H to form the hologram function $\mathcal{H} : \Gamma_H \to \mathbb{C}$. The positions of the measured points must be spaced no farther than $\lambda/2$.

III. Imaging Scheme

The imaging principle aims to reconstruct the reflectivity $\mathcal{R}$ on a plane inside Ω_2. A classical approach for holographic GPRs is the so-called Conjugated-Phase Matching filter (CPM) [2]. CPM allows for improved cross-resolution with computational complexity compatible with real-time applications, and relies in the computation of propagation round-trip path lengths. These paths are easily computed when only one propagation domain is involved (cf. [1]). The situation changes when propagation occurs in two domains separated by an interface. The computation of the propagation paths, in an optical fashion, can be achieved with a family of filter functions $F_S(\vec{r}, \vec{r}_H)$ once the surface Γ_S is known:

$$\mathcal{R}(\vec{r}) = \int_{\Gamma_H} F_S(\vec{r}, \vec{r}_H)\mathcal{H}(\vec{r}_H)d\Gamma_H(\vec{r}_H).$$

A basic approach to adapted filtering is the application of a phase-conjugated matching filter,

$$F_S(\vec{r}, \vec{r}_H) = e^{-\mathrm{i}2\pi\frac{\ell_S}{\lambda}},$$

where the optical round-trip can be computed in accordance to Fermat's Principle in an optical approximation. The validity of this approximation will vary with the wavelength λ, the electrical permittivity ε_2, and the size of the features of surface Γ_S. For $\vec{r}_H \in \Gamma_H$ and $\vec{r} \in \Omega_2$, and given a known (after LIDAR scanning) surface, we consider the minimal round-trip optical path length

$$\ell_S = \ell_1^g + \ell_1^r + \sqrt{\varepsilon_r}\left(\ell_2^g + \ell_2^r\right),$$

where $\ell_1^g + \sqrt{\varepsilon_r}\ell_2^g$ is the minimal optical path length between the emitting point $\vec{r}_H$ and and a point $\vec{r}$ in the imaging plane, the *go* trip, and $\ell_1^r + \sqrt{\varepsilon_r}\ell_2^r$ is the minimal optical path length for the *return* trip. Fig. 2 illustrates the paths for a couple of measuring and imaging points.

Further filtering approaches, not used for the presented results, consider the application of phase-conjugated matching filter that takes into account the propagation across the whole surface Γ_S as the parameters involved further violate the assumptions of Fermat's principle:

$$F_S(\vec{r}, \vec{r}_H) = \int_{\Gamma_S} g(\vec{r}_H, \vec{r}_S)h(\vec{r}_S, \vec{r})d\Gamma_S(\vec{r}_S),$$

where g and h are functions governing wave propagation from the hologram to the interface surface, and from the interface surface into the subsurface domain.

IV. Experimental Setting

In the experimental setting the propagation domain Ω_2 consists of material filling a movable metallic container with the following approximate dimensions: 220cm long, 180cm wide and 70cm deep. A set of 64 antennas separated by 6cm form an antenna array placed 282cm above ground. The movement of the metallic container passing under the antenna array at a constant speed v is recorded during a total time T forming the synthetic scenario described in Fig. 1. In the experimental setting, the surface Γ_H is a rectangular plane located 282cm above the ground, being 378cm (63×6cm) wide and vT meters long. The surface Γ_S separating the air Ω_1 from the soil material Ω_2 is measured by a LIDAR telemetry scanner placed next to the antenna array.

A. Basic Prototype Specifications

The used prototype consists mainly of an antenna array and a LIDAR scanner. The array consists of 64 Vivaldi antennas designed to transmit and receive at a frequency $f = 2.41$GHz. The antennas are channeled through a cascade of radio frequency switches to an In-phase and Quadrature demodulator and to a voltage-controlled oscillator through a circulator. The commutation speed of the cascade is $T_c = 25\mu$s per antenna, thus the theoretical maximum speed of the radar (or the passing metallic container) is 10km/h (approximately 2.7 meters per second) in order to respect a maximum distance of $\lambda/2$ between measured samples.

V. Simulated Results

In this section, reflectivity images are reconstructed using the proposed method with data obtained in numerical simulations based on boundary integral methods.

A. Simulation Environment

In the simulation environment, Γ_H is a rectangular plane placed at 282cm above the ground ($z = 0$cm):

$$\Gamma_H = \{(x, y, z); -1\text{m} \le x, y \le 1\text{m}, z = 2.82\text{m}\}.$$

The interface Γ_S used in simulations is a rippled surface to illustrate the imaging capabilities in non-flat interfaces. The surface is placed in simulations at 1.6 meters above the ground, resembling the height later used in physical experiments with the metallic container.

B. Target

The target model for Ω_3 used in simulations is an L-shaped metallic screen of dimensions 30cm$\times$30cm. In simulations, the target Ω_3 is placed 10cm beneath the interface surface Γ_S, which is placed 160cm higher than the ground (z =0cm). Fig. 3 shows the computational mesh computational model of the target Ω_3 used in the simulations.

C. Simulation Results

Fig. 5 shows the magnitude of the reconstructed reflectivity $|\mathcal{R}|$ using the rippled surface Γ_s depicted in Fig. 4. As seen on the figure, shape reconstruction allows for the identification of the proposed target model used in the simulation.

VI. Experimental Results

In this section we present the results obtained using the experimental setting and the prototype described in Section IV.

A. Soil Material Ω_2

The material used in the experiment reported is a soil mixture made of rocks ranging in size from powder to 30cm wide. This violates the homogeneity assumption specified in Section II, and thus represents a significant challenge for the imaging technique, but it provides a realistic application example. Fig. 6 shows the soil material inside the container used in the experiments.

B. Target

The target used in the presented experiment is a 50cm$\times$50cm metallic plaque buried approximately 10cm below the surface Γ_S of the soil material.

C. Experimental Results

The experiment was executed moving the metallic container under the antenna array at a constant speed v =1.8m/s. The LIDAR scanner measured the surface Γ_S of the material inside the container, and the antenna array and associated electronics measured the hologram $\mathcal{H}$. The application of the described imaging scheme using the hologram, and the measured surface Γ_S, allowed for the reconstruction of the reflectivity $\mathcal{R}$ in a plane at z =150cm approximately in a zone where the target was known to have been buried. Fig. 7 shows the measured surface Γ_S and the reconstructed reflectivity showing the presence of the buried reflector within the described heterogenous material.

VII. Conclusion

An extension to the Conjugated-Phase Matching imaging scheme, applicable to airborne GPR in zones of irregular surface, has been presented. Imaging capabilities have been tested via simulation. Experimental results have been presented in a realistic and challenging scenario under realistic conditions, namely with a flyby speed $v = 1.8$m/s of an antenna 1.2 meters over the surface interface to produce reflectivity images of targets buried 10cm in heterogenous materials.

Acknowledgements

This work was partially supported by MECE Educación Superior (2) PUC0710, the labex LMH through the grant no ANR-11-LABX-0056-LMH in the "Programme des Investissements d'Avenir" and Project CYTED 712RT0449 "Métodos Avanzados para la Visualización del Subsuelo".

References

[1] L. Giubbolini, and L. Sambuelli, *New developments in ground probing radar: the possibility of reconstructing a holographic image of underground reflectivity*, in *Annals of Geophysics* Vol. 43, Num. 6, 2000.

[2] D. Mensa, *High resolution radar cross-section imaging* Boston MA, Artech House, 1991.

[3] S. I. Ivashov, et al., *Holographic subsurface radar of RASCAN type: Development and applications* in *IEEE Journal of Selected Topics in Applied Earth Observations and Remote Sensing* Vol. 4, Issue 4, 2011.

[4] L. Capineri et al., *Comparison of GPR sensor types for landmine detection and classification*, in *12th International Conference on Ground Penetrating Radar*, Vol. 55, 2008.

[5] V. V. Razevig, et al., *Advantages and restrictions of holographic subsurface radars* in *IEEE 13th International Conference on Ground Penetrating Radar*, 2010.

[6] L. Qu et al., *Diffraction tomographic imaging algorithm for airborne ground penetrating radar*. in *15th IEEE International Conference on Ground Penetrating Radar (GPR)*, 2014.

[7] I. Catapano et al., *Airborne ground penetrating radar imaging of buried targets: A tomographic approach*, in *6th International Workshop on Advanced Ground Penetrating Radar (IWAGPR)*, 2011.

[8] D. J. Daniels, *Surface-penetrating radar*, in *Electronics & Communication Engineering Journal* Vol. 8, no. 4, 1996.

[9] S. Ivashov, et al., *Holographic subsurface radar for diagnostics of cryogenic fuel tank thermal insulation of space vehicles*, in *NDT & E International*, vol 69, 2015.

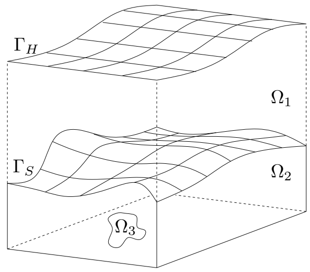

Fig. 1. General setting for a holographic GPR: a surface Γ_H where the hologram $\mathcal{H}$ is recorded, and the surface Γ_S separating two propagation domains.

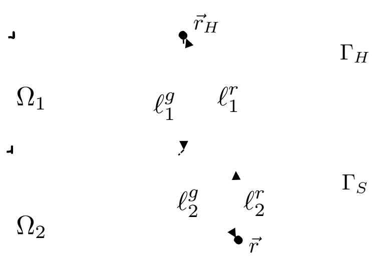

Fig. 2. Path diagram for a point $\vec{r}_H$ if the hologram $\mathcal{H}$ and a subsurface point $\vec{r}$.

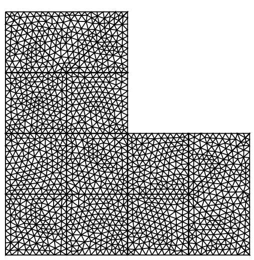

Fig. 3. Computational mesh model of a 30cm x 30cm L-shaped target consisting of 2866 triangles used in simulations.

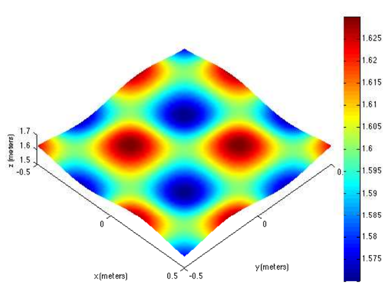

Fig. 4. Rippled surface Γ_S used in simulations.

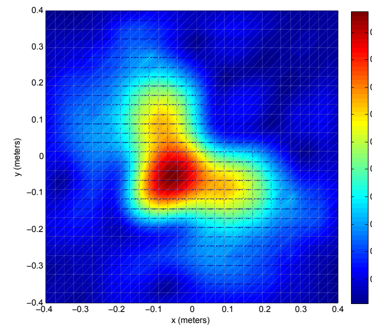

Fig. 5. Magnitude of the reconstructed reflectivity $\mathcal{R}$ using the rippled surface Γ_s depicted in Fig. 4 and using the described L-shaped target depicted in Fig. **??**.

Fig. 6. Photo a the soil material used in the experiments inside the metallic container. Different sizes of rock can be seen making up the propagation domain Ω_2.

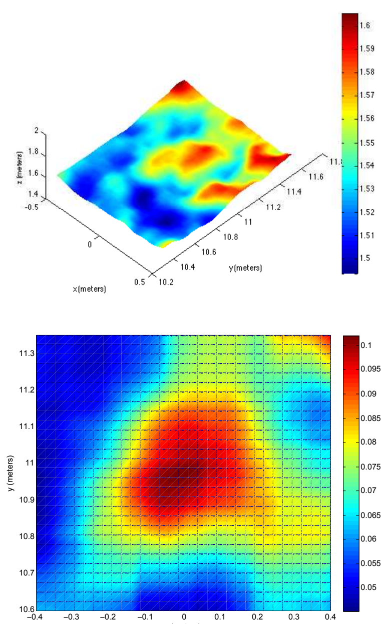

Fig. 7. The measured surface Γ_S (top) and the magnitude of the reconstructed reflectivity (bottom) showing the presence of the buried reflector (a 50cm$\times$50cm metallic plaque) within the described heterogenous material.